Available online at www.sciencedirect.com

jmr&t Journal of Materials Research and Technology

journal homepage: www.elsevier.com/locate/jmrt

Original Article

Mechanical, stress corrosion cracking and crystallographic study on flat components processed by two combined severe plastic deformation techniques

L. Romero-Resendiz [a], J.M. Cabrera [b], S. Elizalde [b], V. Amigó-Borrás [c], I.A. Figueroa [a], G. Gonzalez [a,*]

[a] Instituto de Investigaciones en Materiales, Universidad Nacional Autónoma de México, Circuito Exterior S/N, Cd. Universitaria, A. P. 70-360, Coyoacán, C.P. 04510, Mexico

[b] Departamento de Ciencia e Ingeniería de Materiales, EEBE – Universitat Politècnica de Catalunya, Eduard Maristany 10-14, 08019, Barcelona, Spain

[c] Universitat Politècnica de València, Instituto de Tecnología de Materiales, Camino de Vera S/n, 46022, Valencia, Spain

ARTICLE INFO

Article history:
Received 3 December 2021
Accepted 2 March 2022
Available online 12 March 2022

Keywords:
Al–alloy
Repetitive corrugation and straightening
Accumulative roll bonding
Stress corrosion cracking
Texture
Mechanical behavior

ABSTRACT

Although the current field of application of Al–alloy 7075 (AA7075) is vast, it is still limited due to some drawbacks, especially due to its susceptibility to stress corrosion cracking (SCC). This work aims to evaluate the microstructural, mechanical, and stress corrosion cracking (SCC) behaviors on an AA7075 in flat format deformed by a combination of repetitive corrugation and straightening (RCS) and accumulative roll bonding (ARB) techniques. Four different deformation routes were applied, namely: ARB (A), RCS (R), RCS + ARB (RA) and ARB + RCS (AR). As expected, the efficiency for grain refinement depends on the applied route, in terms of average grain size regarding the initial condition IC): AR > A > RA > R. All conditions resulted in unimodal and widened grain size distributions of micro-, submicro- and nano-metric dimensions. The study of crystallographic orientations showed that route R did not generate any new texture, whereas different preferred orientations were obtained for routes A, RA, and AR. The hardness and three-point bending tests showed an improvement of mechanical strength in the following order: AR > RA > A > R. The cracks per cm^2 obtained in the corrosion study indicated that the best SCC resistance was R > A > AR > RA. Based on the above, the best combination of microstructural, mechanical, and SCC properties until one deformation pass was obtained by the single route of the ARB process.

* Corresponding author.
E-mail address: joseggr@unam.mx (G. Gonzalez).

https://doi.org/10.1016/j.jmrt.2022.03.010

1. Introduction

Flat components of Al alloys with distinct geometries are highly used in several industries, such as aeronautic, naval, automobile bodies, machinery, and equipment, storage tanks, cans, among others [1,2]. In 2018, the global Al-based alloys flat products market size exceeded USD 52 billion and the growing estimations are over 5.0% of the compound annual growth rate for the period between 2019 and 2026 [3]. From the abovementioned flat products, the 7075 Al–alloy (AA7075) is commonly applied in aircraft parts, particularly in wing coating, spars, and stabilizers, as well as in machinery and equipments, due to its high mechanical strength, high strength-to-weight ratio and fatigue resistance [4]. However, the field of application of the AA7075 is still limited for some drawbacks, such as its susceptibility to stress corrosion cracking (SCC).

To overcome the previous problem, a few authors have reported the improvement of SCC susceptibility on AA7075 through superficial severe plastic deformation techniques (SPD) as laser peening [5,6]. This result is related to the generation of a compressive stress state that delays cracking formation and propagation [7–9]. However, these efforts have been addressed to superficial studies and not to the entire volume of the material. Repetitive corrugation and straightening (RCS) and accumulative roll bonding (ARB) are two promising techniques of the SPD family, which were designed for flat geometries. Both processes induced compressive stress state [10,11] and are highly efficient to refine bulk Al-based microstructures to submicro-metric or nano-metric sizes [12–17]. As result, ARB and RCS materials have enhanced mechanical properties [16,18–22] in comparison with their coarse-grained counterparts. Moreover, the ARB process has improved the electrochemical corrosion susceptibility of Al–Mn and Al-1050 alloys [23,24]. This was explained in terms of residual stress and defects that create better conditions for continuous and adhered passive films. Besides, the RCS process has been shown not to aggravate resistance to SCC in an Al-7075 alloy with broad grain sizes distributions [18]. From the above, RCS and ARB processes could increase the shelf life of the abovementioned applications of AA7075 flat-made components as automobile carcass, pressure vessels, chemical containers, aircraft parts, ship body components, machinery, architecture, among others [18,25]. However, none of the previous works has studied the relationship between mechanical – microstructural – crystallographic features and their effect on the corrosion behavior of these alloys. It is well known that microstructure and preferred orientation significantly impact the mechanical assessment of metallic materials. Studying the relationship between them is fundamental for a good understanding of the final performance. It is widely reported that RCS and ARB processes reduced the grain size and improved mechanical properties since the first deformation pass [14,17,25,26]. Accordingly, this work focuses on studying the first pass of deformation by each of the abovementioned routes. The need for a single deformation pass could be advantageous for many applications due to the cost-effective process, the requirement of low labor demands, and high-volume production.

This work aims to study the microstructure, texture, and mechanical response generated by the application of RCS and ARB and their combination on an AA7075. The results were correlated to the SCC susceptibility of the processed alloy. The comparison between four deformation routes (RCS, ARB, RCS + ARB, and ARB + RCS) allowed determining the most effective path for improving the mechanical assessment without affecting the SCC of the AA7075. To date, no previous literature specifically studying the SCC susceptibility or texture performance of the AA7075 processed by a combination of RCS and ARB processes has been reported. The results of this work might reduce the current limitations of the AA7075 and broaden the knowledge of flat Al-based alloys processed by SPD techniques.

2. Experimental procedure

A commercially available AA7075 in T4 condition from "*La Paloma Compañia de Metales*" was used as starting material. The chemical composition of the alloy was Al-5.3Zn-2.2Mg-1.8Cu-0.3Fe-0.28Cr-0.06Ti-0.01Ni (wt.%). The supplied plates had a thickness of 12.5 mm, but they were subjected to cold-rolled down to a thickness of 1 mm. A heat treatment at 450 °C for 2 h and slow cooling in the furnace down to room temperature (RT) was applied to obtain an initial homogeneous texture on the sheets of 1 mm in thickness, 120 mm in width, and 120 mm in length. These samples are identified in this work as the initial condition (IC).

2.1. *Plastic deformation processing*

2.1.1. *RCS processing*

The IC samples were further processed by RCS at room temperature. An Instron 8802 hydraulic press with a maximum capacity of 200 kN was used for this purpose. Polytetrafluoroethylene sheets of 0.39 mm thickness were used to minimize the friction coefficient between the sample and the RCS dies. The geometry of the two D2 steel dies based on sinusoidal profiles for the corrugation stages can be observed in Fig. 1a. The straightening steps of the RCS process were carried out between two flat dies. The processed sheets were rotated 90° around the normal direction to alternate the most deformed zone between each corrugation stage. For this work, each RCS pass consists of 5 stages: 1) corrugation – 2) straightening – 3) 90° rotation – 4) corrugation – 5) straightening. As a result, all sheets are flat at the end of each RCS pass. The effective strain for each RCS pass using the design shown in Fig. 1 was equal to ~0.8, in the most deformed zones [17]. It is worth mentioning that two of those flat sheets were cleaned, brushed up, and piled up before being subjected to the ARB process (as explained below).

2.1.2. *ARB processing*

The IC sheets were brushed and cleaned with acetone before the deformation process. ARB was performed at 300 °C at a compression rate of 0.5 m s^{-1}. This temperature corresponds to 0.6 of the homologous temperature, which is above the range of cold working for Al-based alloys [27]. The selection of this temperature facilitated the passage of the strips

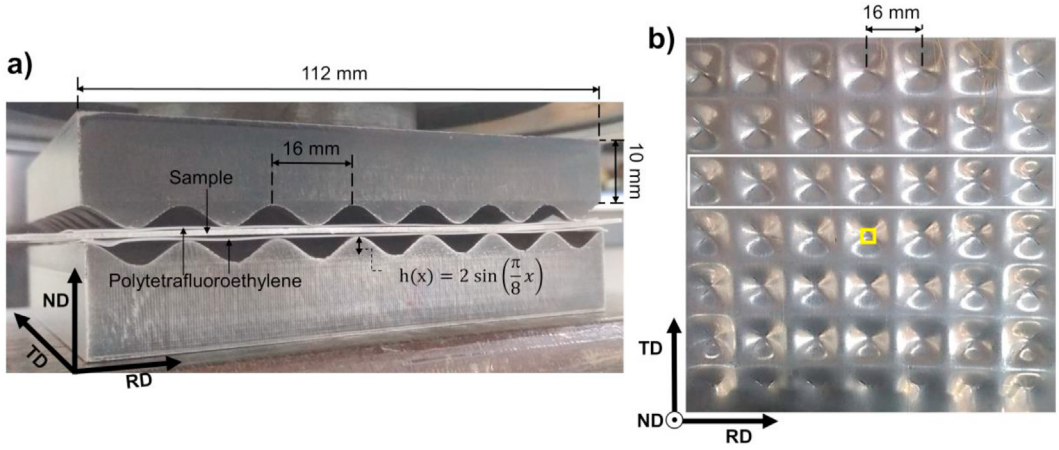

Fig. 1 – a) Corrugation RCS die used in this work and b) site where the samples were taken for the characterization. In white and yellow, the location of samples for bending and all the rest studies, respectively. ND, TD, and RD are the normal, transversal, and rolling directions, respectively. h(x) is the height, and x is the horizontal coordinate.

through the laminating rollers, activating the diffusion mechanisms that allow the mechanical union between the plates. Before the rolling processing, the sheets (consisting of two stacked IC strips) were pre-heated for 15 min. This methodology was based on previous literature reports [14,28]. For the present work, a deformation pass by ARB refers to the following 2-stage process: 1) stacking of two IC strips, 2) single lamination with a 50% reduction in thickness. Considering the reduction in thickness per pass, the equivalent deformation (ε) estimated for each ARB processing step is ~0.8 [29].

2.1.3. *RCS mixed ARB processing*

For the combination of deformation techniques, both processes were carried out following the methodology described in 2.1.1. and 2.1.2. Subsections. The processed samples were identified as R, A, AR, and RA, where the letters R and A correspond to one pass RCS and ARB processes, respectively. The sequence of the letters indicates the order of application of the processes.

2.2. *Microstructural evaluation*

X-ray diffraction (XRD) measurements were performed using a Rigaku Ultima IV diffractometer, with Cu-Kα radiation, crossbeam optics (CBO), operating at 40 kV and 44 mA. A step size of 0.02° and a scanning speed of 0.07° min^{-1} were used for peak broadening measurements. Moreover, a sampling step of 1.5° and a scanning speed of 100° min^{-1} were used for texture measurements (α: 0–90°; β: 0–360°).

The macro residual strain (ε) was estimated using the slope of ε versus $\sin^2\psi$, where ψ is the angle formed between the normal of the sample and the normal of the diffraction plane. The (422) plane and 10 experimental ψ values (from −60° to 54°) were taken for each curve. The measurements were done on the raw surface of the IC, R, and A samples.

For the electron backscattering diffraction (EBSD) analysis, the AA7075 samples were prepared by standard metallographic preparation and finished by vibratory polishing (VibroMet 2), using a colloidal silica solution with a particle size of 0.3 μm. The EBSD analysis was carried out in a Jeol JSM-7001F scanning electron microscope (SEM) with a Bruker Quantax EBSD detector (15 KV). Based on the experimental EBSD results, orientation distribution functions (ODF) were calculated with MTEX 5.6 software (MATLAB toolbox R2020b) [30].

2.3. *Mechanical behavior*

The processed samples were cut along the rolling direction into bone-shaped specimens. The tested samples sized 12.5 mm in gauge length, 3.3 mm width, and ~1 mm thickness after SiC grinding until 2000 grade. Uniaxial tensile tests were performed on a universal testing machine (Instron 3382,100 kN) with a strain rate of 10^{-4} s^{-1} at RT. Three samples of each studied condition were tested. The yield strength was determined at the 0.2% strain. The end of the uniform elongation was determined by the Considère criterion [31].

For determining the bending stress applied during the SCC tests, three-point bending tests were performed utilizing a Shimadzu AGX universal testing machine. Results were recorded and plotted with the TrapeziumX software. The bending load was applied by exerting a concentric load on the center of the rectangular geometries described in Table 1. The span between both supports, as well as the diameter of punch and supports, are also shown in Table 1. The bending rate was 2 mm min^{-1}.

A Shimadzu microdurometer model HMV-FA2 with an applied load of 100 gf for 10 s was used to evaluate the hardness of the samples. An average of 10 microhardness measurements were taken per sample.

2.4. *Stress corrosion cracking evaluation*

The surface of three samples from each condition (IC, R, A, RA, and AR) was cleaned with acetone before the SCC testing. The samples with the geometry dimensions specified in Table 1

Table 1 – Samples dimensions and employed parameters for bending test.

Sample	Thickness/mm	Width/mm	Length/mm	Span between supports/mm	Diameter of punch and supports/mm
IC	1.0	16.0	115.0	100.0	5.0
R	1.0	16.0	115.0	100.0	5.0
A	1.0	10.0	60.0	50.0	5.0
RA	1.0	10.0	35.0	25.0	2.5
AR	1.0	10.0	35.0	25.0	2.5

were immersed in a 3.5 wt. % NaCl solution for 168 h at RT. Constant flexural stress equal to 1 and 1.2 times the yield strength (YS) was applied on all samples. The length of the tested samples was parallel to the rolling direction. The SCC study was carried out following the standard ISO 9591 [32]. After testing, samples were prepared by conventional metallographic procedures until mirror finishing appearance with a diamond solution of 0.1 μm in particle size. Optical microscopy observations were carried out to evaluate the cracking morphology and quantification. The standard deviation from the mean values was estimated considering the three measurements per condition.

3. Results and discussion

3.1. *Microstructural evaluation*

Figure 2 shows the EBSD inverse pole figures (IPF) micrographs of the IC, R, A, RA, AR samples, as well as the orientation map key. A substantial microstructural evolution after the ARB process can be observed. According to the color orientation map key, IC and R samples showed preferred orientations to the [001] and [101] directions, the A sample to the [111], and the RA and AR samples to more complex orientations. The IC and R (Fig. 2a,b) samples showed some of their crystals with

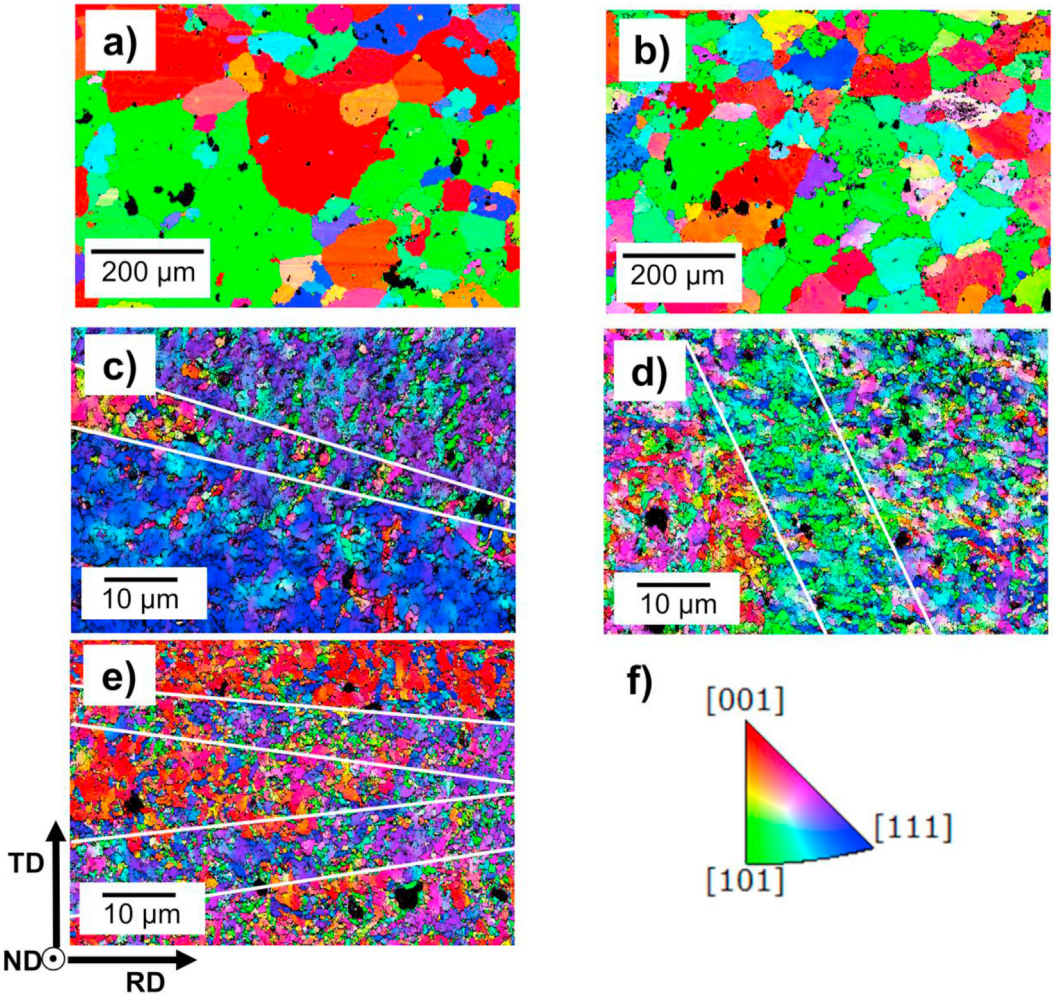

Fig. 2 – EBSD IPF micrographs in the normal direction (ND) for a) IC, b) R, c) A, d) RA, and e) AR samples and f) orientation map key. Deformation bands were indicated by white solid lines.

<100> parallel to the ND, i.e., in the cube texture typically obtained from recrystallization processes as the homogenization applied to the IC sample [33]. This suggests that the deformation induced by 1 RCS pass was not enough to cause a significant microstructural evolution. The visible lower grain refinement supports the previous statement in the R sample compared to the A, RA, and AR. This was totally expected due to the largest "ε" applied in the overall sample by ARB (ε~0.8) compared to that of the RCS process (0.003 < ε < 0.808) [17,29]. From Fig. 2c, the high crystals density, parallel to the ND and oriented to <111> in the sample A is similar to the reported for the AA7075 processed by one hot-ARB pass [14]. This copper-type texture can be expected for rolled high stacking fault energy (SFE) materials [34], as Al with an SFE of 200 mJ m-2 [35]. This copper-type texture has been related to the dominant cross slip deformation mechanism in high-SFE FCC metals [34,36]. From the combination of deformation techniques, more complex textures were obtained. Furthermore, the micrographs of Fig. 2 display a severe grain refinement, especially when the ARB process is applied (samples A, RA, and AR). As a result of the higher equivalent strain applied with the ARB to the AA7075, deformation bands were observed in samples A, RA, and AR. Similar coarse deformation bands have been reported in the AA7075 under equivalent strain by equal channel angular pressing (ECAP) with a 120° die angular channel [34]. As in the RA and AR samples (Fig. 2d,e), the deformation bands in the AA7075 subjected to ECAP showed no well-defined angles when the deformation increased [37]. The creation of deformation bands with the ARB process might encourage the grain sub-division and provide nucleation sites for new forming grains in Al alloys when further deformation is applied [37,38].

Figure 3 shows the grain size histograms weighted by area for the IC, R, A, RA, AR samples to analyze the grain refinement that occurred after every deformation route Compared to the average grain size of the IC sample (126 μm, Fig. 3a), the order from larger to lower grain refinement produced by the four routes was AR (1.2 μm, Fig. 3e) > A (3.2 μm, Fig. 3c) > RA (3.7 μm, Fig. 3d) > R (83.1 μm, Fig. 3b). The obtained grain refinement by 1 RCS pass in the AA7075 was similar to the obtained in AA6061 processed under same conditions [17]. However, the grain refinement in the A sample

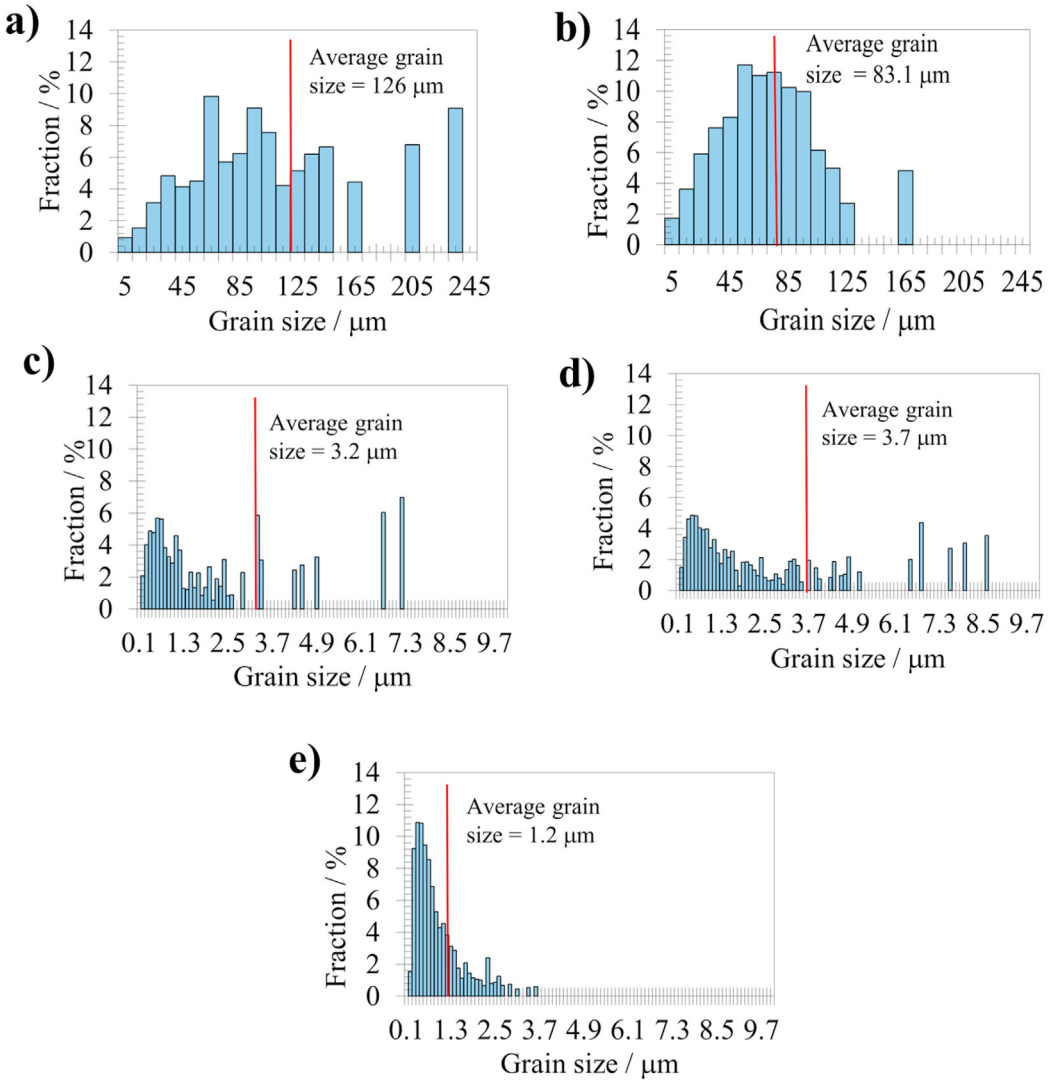

Fig. 3 – Grain size histograms weighted by area for a) IC, b) R, c) A, d) RA, and e) AR samples.

was lower than the reported in the literature for AA7075 processed by 1 ARB pass [14], which reached a grain size average of 440 nm. This difference could be related to the higher ε per pass (~1.1) reported in the literature [14] compared to that applied in this work (~0.8). Furthermore, the ε for the combination of RCS and ARB in the samples RA and AR is of ~1.0 for the less deformed zones to ~1.6 for the most deformed zones. Compared with the grain size reduction of about 98.9% (considering the final grain length) after two ECAP passes (ε~2.0) in the AA7075 [39], the grain size reduction of 97.0 and 99.0% for the RA and AR samples is similar. This suggests that the heterogeneous nature of the deformation applied by the RCS process might not be so significant in terms of grain refinement.

It is noteworthy that the grain size distribution of the IC and R samples are unimodal and nearly symmetrical. However, the distribution profiles are unimodal and asymmetrical with right-skewed distributions in samples A, RA, and AR. Besides, a large percentage of grains in the samples where the ARB process was applied were below the sub-micrometric range (1 μm). It is also remarkable that the coexistence between sub-micrometric and micrometric grain sizes in all samples, especially in A, RA, and AR, were almost homogeneous throughout the samples. The finest grains are distributed randomly through every microstructure without forming colonies or clusters. A bigger grain size average in the RA sample compared to the AR was also observed. This could be related to the probable dynamic recovery occurrence due to the process temperature employed for ARB. The RA sample received a stimulus (temperature) on an already high-dense defects structure, increasing the probability of partial-dynamic recovery. The occurrence of dynamic recovery in AA7075 processed under similar conditions (warm ARB process at ~350 °C) has been reported before [14]. On the other hand, the final microstructure of the AR sample retained the effect of the last deformation step.

Figure 4 shows the correlated misorientation histograms, uncorrelated misorientation profiles (red line), and the distribution of grain fractions for certain ranges of misorientation of the IC, R, A, RA, and AR samples. The uncorrelated profiles (or texture derivatives profiles) do not assume a spatial correlation between pixels, i.e., they account for all possible misorientations, including those between points that are not adjacent to each other (even between different grains). These profiles show the effects of transgranular strain, such as grain rotations or the formation of new grains. The correlated histograms result from the angle measurements between contiguous pixels, resulting in a high density of misorientation values lower than 5°. Considering that the largest fraction of the area of the samples belongs to the interior of grains and not to the borders, the histograms were plotted since 5° of misorientation. The correlated and uncorrelated profiles of the IC sample have similar tendencies, indicating that within the grains and in their neighborhood, there is a similar misorientation. This means that the IC sample is practically free of substructures or lineal defects that could noticeably vary the misorientation. The correlated and uncorrelated profiles also showed a large similarity on the R sample, which indicates again that the microstructural evolution until one RCS pass is not enough to alter the crystalline domains of the sample significantly. This is congruent with the low grain refinement obtained on the R sample. Nonetheless, after the AA7075 was subjected to the ARB process, the differences between both misorientation profiles became clearer. This could be an indication of the presence of subgrains, resulting from the polygonization process that controls the substructures or from twins formation. However, considering that twinning is rarely observed in aluminum due to its high stacking fault energy [40], it can be considered that these misorientation profiles differences are related to polygonization. The above can be understood as a substantial difference in the misorientation of the individual grains and the whole sample, i.e., intra- and inter-granular strain, which in turn could be linked to the grain size distributions. The grain size histograms showed ranges from sub-micrometric to micrometric on the A, RA, and AR samples, indicating that, while some dislocations have already formed subgrains, several others are being continuously accumulated.

From the distribution of misorientation fraction in all samples illustrated in Fig. 4f, the IC sample showed 90.2% of misorientation boundaries greater than 15°, i.e., high angle grain borders (HAGB). The high density of HAGBs is consistent with the micrometric and stress-relieved microstructure resulting from the homogenization heat treatment. Despite the grain refinement shown from the grain size histograms, the R sample presents more than 90% of HAGBs. This indicates that up to one RCS pass, the formation of substructures does not occur in high density. On the other hand, when the ARB process was applied (A, RA, and AR samples), less than 50% of borders were considered HAGBs, agreeing with the largest grain refinement promoted by ARB. The increment of low angle grain boundaries (LAGBs) i.e., boundaries with misorientations below 15°, after applying the ARB process is a clear indication of the subgrain formation [13], which is also in agreement with the differences between correlated and uncorrelated profiles. The presence of HAGBs in the A, RA, and AR samples, is a positive indicator of ductility without a high sacrifice of mechanical resistance in various alloys [41,42]. This phenomenon has been explained in terms of the accumulation of linear defects, leading to polygonization and new LAGBs. Such new LAGBs will absorb dislocations and later become HAGBs [43,44], decreasing the dislocations density and allowing ductility in the material.

Figure 5 shows the IPF in the normal direction (ND) and representations of the high-density oriented crystals for the IC, R, A, RA, and AR samples. Compared to the IC sample (Fig. 5a), the higher dense crystals positions mainly oriented to the <001> and <011> directions in the R sample are almost similar (Fig. 5b). This is congruent with the low grain refinement, and the similarity between correlated and uncorrelated profiles of IC and R observed in Fig. 4. After applying the ARB process, a high density of crystals rotated to different positions. The A sample is characterized by the highest density of preferred oriented crystals on the <111> direction that is parallel to the ND of the sample (Fig. 5c). Otherwise, the largest density of crystals on the RA sample is oriented to the <-3 7 11> direction (Fig. 5d), while a high density of crystals is oriented towards the <-1 1 2> and <-1 1 7> directions (Fig. 5e) in the AR sample. The evolution of crystallographic texture

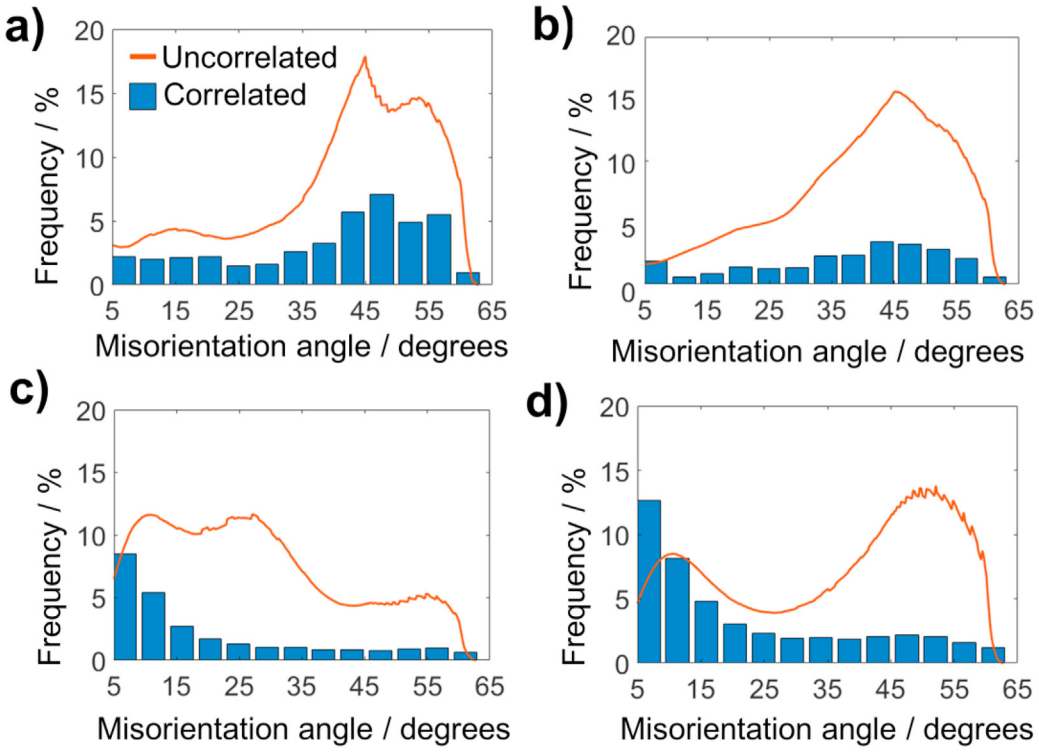

f)

Sample	Misorientation / degrees		
	2.0-5.0	5.0-15.0	15.0-61.7
IC	0.5	9.3	90.2
R	0.9	5.2	93.9
A	10.6	52.0	37.4
RA	6.9	48.8	44.2
AR	6.6	42.9	50.4

Fig. 4 – Correlated misorientation histograms and uncorrelated misorientation profiles for a) IC, b) R, c) A, d) RA, and e) AR samples, and f) distribution of correlated misorientation angles for the same samples.

when the ARB process is apply (A, RA and AR samples) agrees with the observation of deformation bands (Fig. 2), which origins from crystallographic rotation occurrence [38,45]. It is worth mentioning that the texture intensity decreased with the applied strain.

The previously explained differences between grain refinement and texture evolution on the four different samples imply that each process has a different effect on the current AA7075. This means that the order and nature of the applied strain alter the microstructural result. This could be due to the different slip systems that were activated by each deformation route. Such slip systems depend on the material's prior stress state, the Schmid factor associated with each crystallographic plane [46,47], and the strain restrictions (for instance, ARB is a plane strain process). The larger the Schmid factor the higher the shear stresses acting on a given slip system, and therefore a greater facility to deform the grain [48]. As the behavior of the grains located several atomic layers below is expected to be different from that on the surface, the previous phenomenon is representative of the surface grains on the material [46]. Therefore, the activation of different slip systems and its dependence on the associated Schmid factor is feasible for the present work in which the zone analyzed by EBSD was superficial.

Figure 6 shows the peak broadening by the differences of the full width at half maximum for the IC, A, R, RA, and AR samples. The profile of the Al-(420) peak on the IC sample observed in Fig. 6a shows the doublet of K-α_1 and K-α_2 contributions, while the convolution of both peaks is not visible for all the deformed samples. This suggested that the grain refinement could be reached down to the sub-micrometric sizes. Considering the typical range of sensibility of the XRD technique, the peak broadening in all the deformed samples (Fig. 6b) is indicative of the formation of nano-metric grains. It

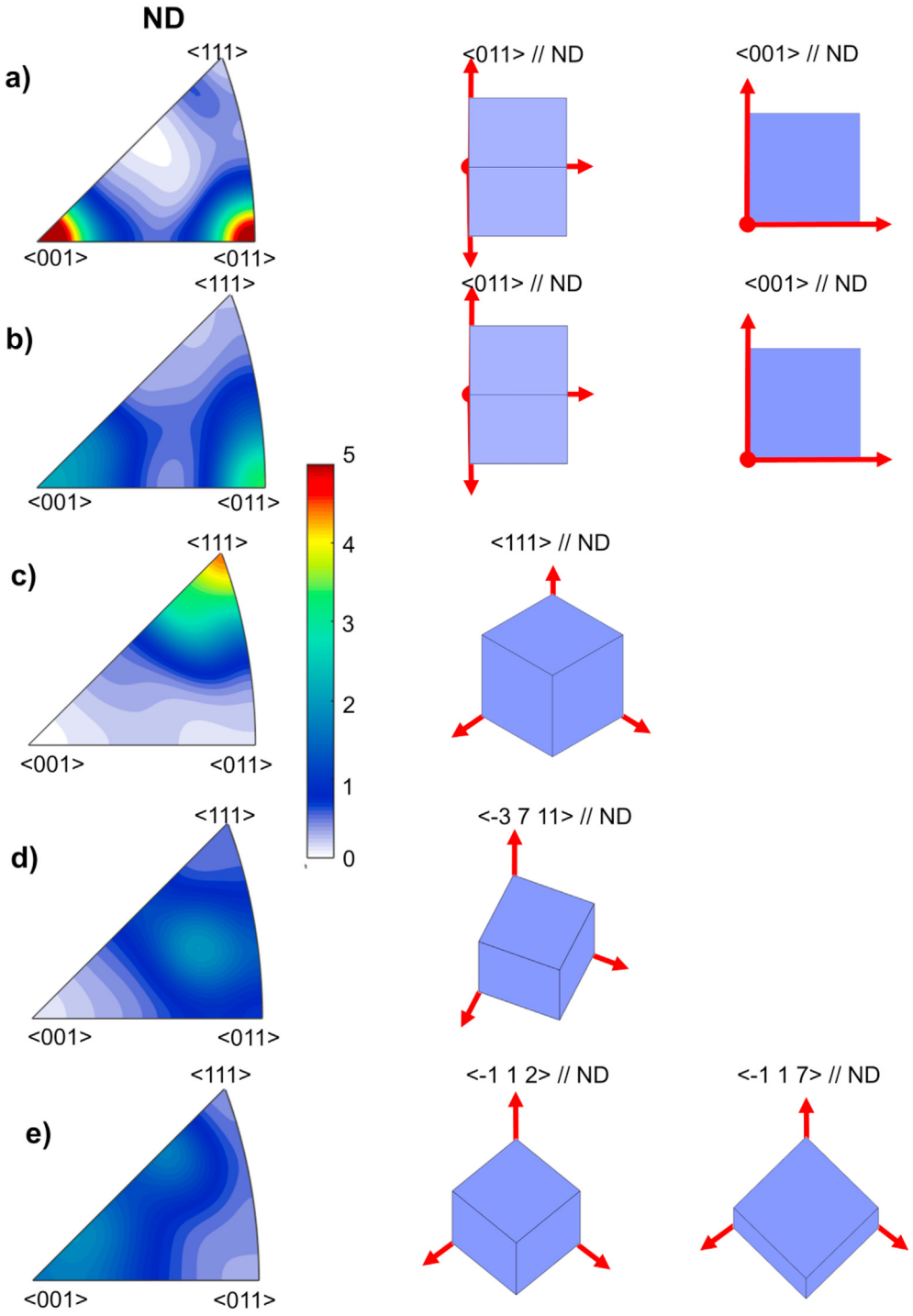

Fig. 5 – IPFs in the normal direction and position of high-density oriented crystals for a) IC, b) R, c) A, d) RA, and e) AR samples.

was also observed the peak shifting from the IC Al-(420) peak for the samples after the ARB process (Fig. 6a). This could be related to the increment of macro-strains in such samples, being congruent with the larger grain refinement (Fig. 3) observed in A, RA, and AR samples in comparison with the R sample. Along with the high grain refinement, the formation of its crystallographic texture, and the suggestion of larger macro-strains, the ARB process causes more significant microstructural changes than the RCS process in the present AA7075.

3.2. *Mechanical behavior*

Tensile test, microhardness, and three-point bending test measurements after applying each deformation route are shown in Fig. 7. The UTS values for the IC, R, A, RA, and AR

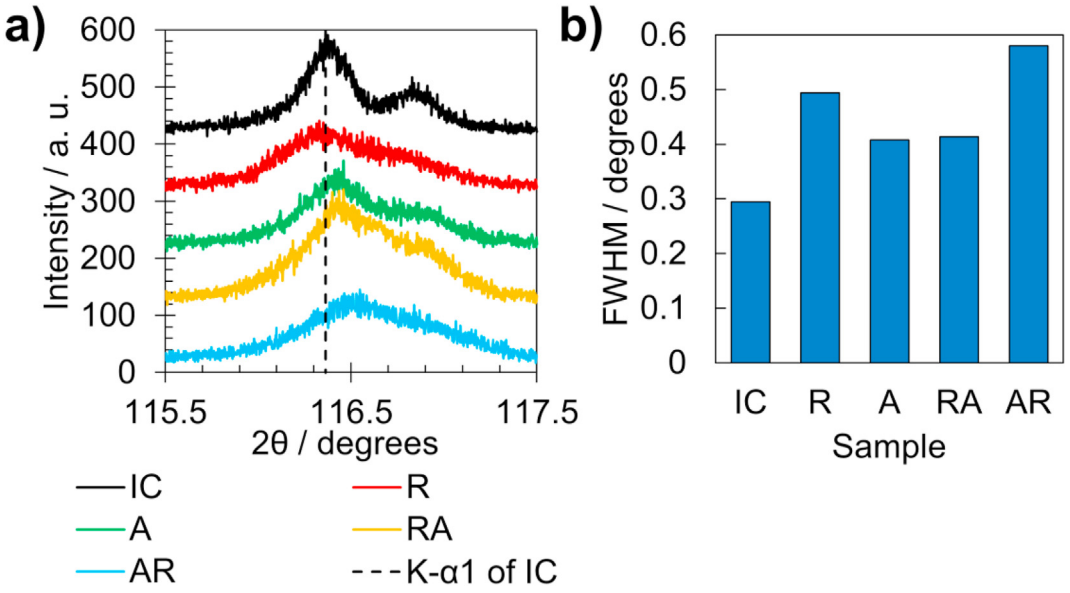

Fig. 6 – Peak broadening for the processed samples by the four different deformation routes employed in this work in comparison with the initial condition sample: a) diffractogram of Al-(420) peak and b) full width at half maximum (FWHM) values for each sample.

samples were 250.6, 217.3, 301.8, 253.7, and 293.2 MPa, respectively (Fig. 7a). The UTS between the A and the AR condition are similar, which was congruent with the higher grain refinement shown in Fig. 3. However, the A condition showed a slightly higher strain hardening rate (Fig. 7b). This suggests a ductility improvement (necking delaying) due to dislocation accumulation in sample A [49]. The higher ductility in sample A was confirmed by a higher uniform elongation (UE) in Fig. 7c. The higher mechanical properties (UTS, YS, and UE) in the samples processed by ARB compared

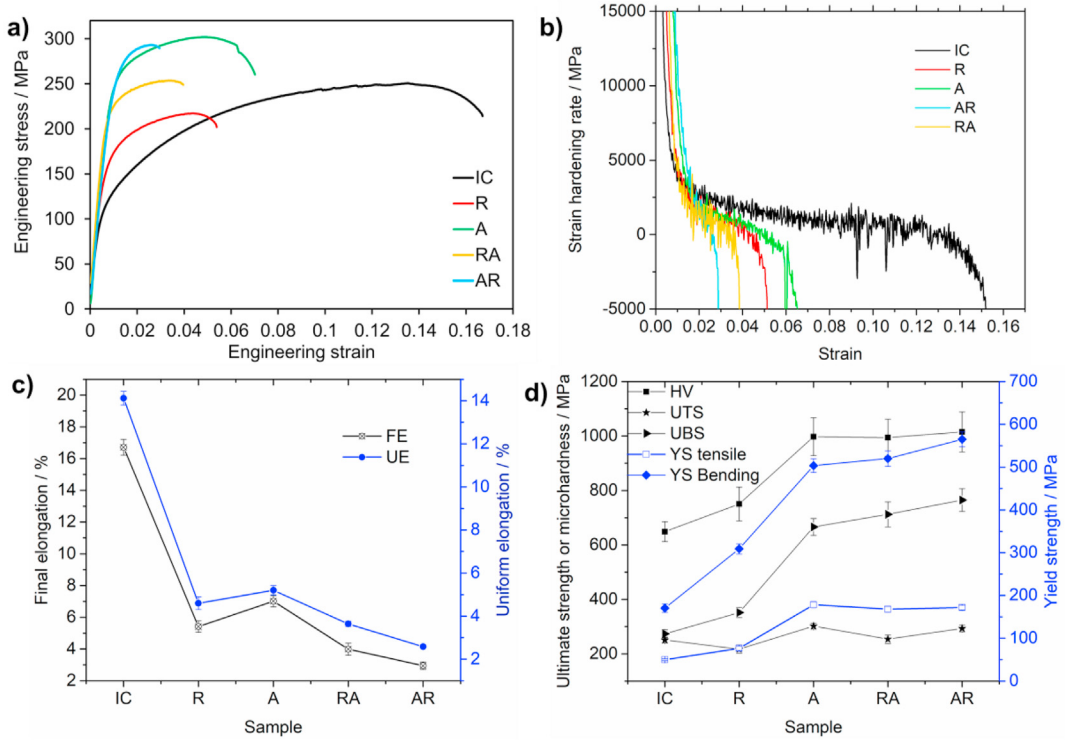

Fig. 7 – Mechanical properties of all samples studied in this work: a,b,c) tensile test and d) microhardness, tensile test, and three-point bending tests. FE, UE, YS, HV, UTS, and UBS refer to final elongation, uniform elongation, yield strength, Vickers microhardness, ultimate tensile strength, and ultimate bending strength, respectively.

to the R sample can be explained in terms of higher applied strain that triggers higher crystallographic evolution (Figs. 4 and 5), formation of deformation bands (Fig. 2), and higher grain refinement (Fig. 3). Therefore, the dislocation accumulation and the creation of deformation bands during the ARB process might assist in incrementing the strain hardening rate and improving the ductility [49,50]. On the other hand, the difference of UTS between the AR and RA samples might be related to possible dynamic recovery, especially in the RA sample. As explained before, the RA sample already had a high dislocation density when heated for the ARB process, increasing the probability of partial-dynamic recovery. The lower UTS of the RA sample compared to that of the AR sample agrees with its lower FWHM from Fig. 6 (bigger crystalline domain) and its larger average grain size (Fig. 3). The higher UTS increment concerning the IC sample was 20.4% for the sample A. This increment was slightly lower than the (83.8, 61.7, and 35.8%) increment of UTS in nanostructured AA7075, related to the coarse, solid solution and the starting condition [39,49,51]. This can be explained in terms of the bigger average grain size of the A sample (3.2 μm). From Fig. 7c, the uniform elongation of A sample (5.2%) is close to that obtained by other SPD techniques such as ECAP [50], and the cryogenically rolled nanostructured AA7075 with and without second phase nanoparticles [49], and to the UFG AA7075 processed by ECAP [51].

Figure 7d shows the comparison between the Vickers microhardness (HV), yield strength (YS) and ultimate strength in bending and tensile tests (UTS, UBS respectively). The HV of all the processed samples increased in comparison with the IC. The percentages of hardness increment were 15.7, 53.8, 53.4, and 56.6% for the R, A, RA, and AR samples, respectively. The grain refinement and substructure formation discussed in Figs. 3b and 4b could produce the hardness increment in the processed samples concerning the IC sample. Compared to the results of this work, a similar hardness increment was obtained in AA1100 (~15.1%) and AA6061 (~16.6%) by using the same sinusoidal die geometry [17,52]. On the other hand, the 53.8% hardness increment in sample A is similar to the reported for the AA7075 processed by 1 ARB pass (~48.3%) [25] under comparable processing conditions.

The YS and UBS increment shown in Fig. 7d indicated a similar trend, especially when the ARB process was involved. YS and UBS increased from 170.5 to 273.3 MPa in the IC sample to a maximum of 565 and 764.7 MPa, respectively, in the AR sample.

From the above, the mechanical properties improvement in the ARB processed samples (A, RA, and AR) are similar. Thus, the selection of the A sample might be advantageous regarding cost-production and scalability of the process. On the other hand, the ARB and RCS processes are not as effective as other SPD techniques e.g., ECAP for improving the mechanical properties. However, the particular microstructure generated by the combination of ARB and RCS techniques might be promising for improving another important requirement of industrial materials, such as the SCC susceptibility.

3.3. *SCC assessment*

Figure 8a–8e illustrates the morphology of representative morphology of cracks of the different studied samples. The IC and R samples (Fig. 8a,b) showed the highest incidence of local corrosion, i.e., pitting. From the application of the ARB process, the pitting fraction is visible lower (Fig. 8c-e). This result agrees with the reports of pitting resistance and passivation layer formation improvements in Al alloys after being processed by the ARB process [23,24]. It has been reported that in the presence of a passivation layer, the high density of defects as grain boundaries and dislocations provide sites for a more compacted, continuous, and well-adhered surface passivation layer [53–56]. Based on the more efficient grain refinement (Fig. 3) and the substantial difference between intra- and inter-granular strain (Fig. 4), the ARB process generated a higher defect density than the RCS process. The previous statement explains the reduction in local corrosion, i.e., less breakage of the surface oxide layer in the samples A, AR, and RA with broad grain size distributions (Fig. 3).

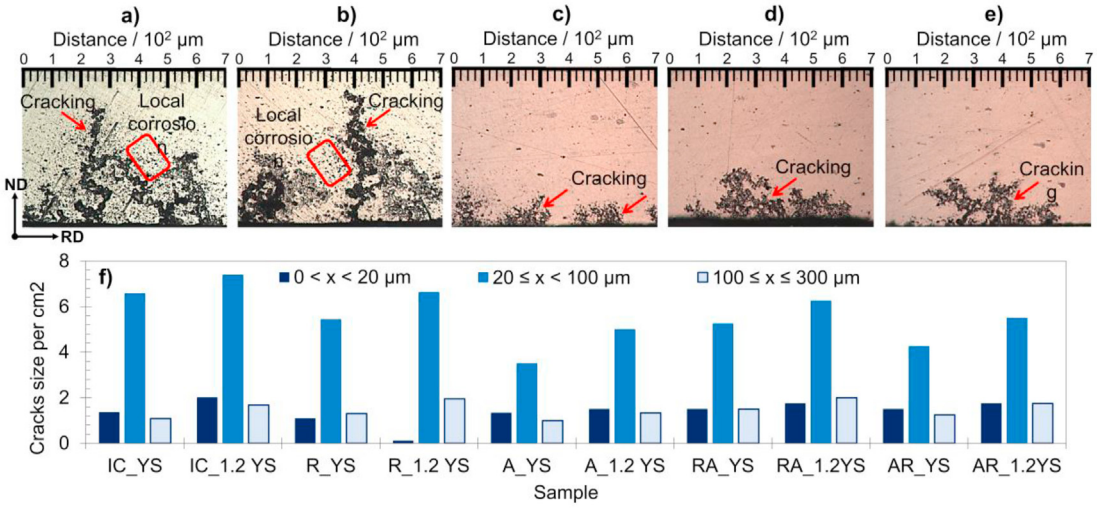

Fig. 8 – Morphology of representative cracks larger than 100 μm obtained under the application of YS in a) IC, b) R, c) A, d) RA, and e) AR samples, as well as f) the size of the cracks per cm² generated in each sample during the SCC tests in the application of 1 (YS) and fold-1.2 (1.2 YS) the yield strength on the processed samples.

Moreover, the ε in the A, AR, and RA samples is higher than that applied to the R sample. In contrast, the ARB pass applied a homogeneous ε~0.8, the ε value ranges from 0.003 to 0.808 in RCS [17], being accumulative for the AR and RA samples. When ε increases, an augmentation of defects and residual stress is also expected.

Compared with the other samples, the IC and R showed the largest cracks. This suggests prolonged cracking initiation in the A, AR, and RA samples compared with the non-deformed and the R samples. Considering that the cracking can be originated from pitting [57,58], the pitting decrement in the ARBed samples might be related to the delay of cracking.

Figure 8f illustrates the size distribution of the cracks per cm^2 from the SCC tests for samples IC, R, A, RA, and AR. The samples were constantly stressed at 1 (YS) and fold-1.2 (1.2 YS) the yield strength. At least the 53% of crack sizes range from 20 to 100 μm for all samples, being the A condition the one with less cracking per cm^2. The R, A, RA, and AR samples displayed 18.2, 42.4, 39.4, and 35.6%, respectively, less density of cracks between 20 and 100 μm under the application of YS in comparison with the IC condition. For the constant application of 1.2 YS, the R, A, RA, and AR samples decreased the density of cracks per cm^2 (between 20 and 100 μm) by 10.8, 18.9, 18.8, and 25.6%, respectively. As expected, the density of cracks on the processed AA7075 increased as a function of the applied stress during the tests.

In comparison with the IC condition, it is thought that the lower cracking of all the processed samples at constant stress equal to YS, might be related to the particular widen and unimodal grain size distributions (Fig. 3). The coexistence of micro-, submicro-, and nano-metric grains through the sample in a well homogeneous distribution of sizes could be compared to a galvanic system with a low chemical potential gradient. The low potential gradients between adjacent grains could be responsible for the decrement of SCC susceptibility of the processed samples. This could be efficiently related to a synergetic mechanism with the formation of a more continuous, adhered, and compacted passive layer in microstructures with a wide range of grain sizes [53]. This is congruent with the slight decrement of SCC susceptibility when larger LAGBs percentage and wider grain size distributions are present in the A, AR, and RA samples. The strong effect of misorientation can also be observed in the small improvement in SCC resistance in the A sample compared to the RA. From Fig. 3, A and RA samples have similar grain size histograms and average grain size, i.e., similar grain boundary length. However, from Fig. 4f, the RA sample has a higher percentage of high-energy boundaries, i.e., HAGBs, compared to the A sample. Considering that HAGBs are preferred sites for dissolution processes in Al [59], this could assist in the small improvement of SCC resistance in A sample compared to the RA. On the other hand, since the texture intensity decreases (Fig. 5) with the equivalent deformation applied, especially after impairing the ARB process, there is no clear relation between crystallographic texture and the SCC susceptibility.

To evaluate the role of residual stress in the decrement of pitting effect on the samples process by ARB, Fig. 9 shows the surface qualitative study of lattice strain. The lattice strain indicated global (first-order) residual stress in the IC, R, and A samples. The IC sample showed a horizontal slope expected

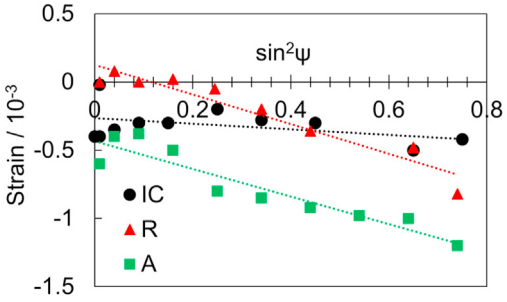

Fig. 9 – Surface tendency of global residual stress generated from RCS (R) and ARB (A) processes, as well as their comparison with the non-deformed (IC) sample.

for stress-relieved materials, but slight compressive values could come from the previous deformation process. Compared to the IC sample, the storage of compressive residual stress increased for the deformed R and A samples. Considering that the R and A samples have similar slopes in Fig. 9, the compressive residual stress magnitude might be nearly similar. However, the A sample showed more negative values. The $sin^2\psi$ model can be related to a more compressive state of the in-plane principal stress [60]. The latter in the ARBed samples support the cracking growth prolongation during SCC tests. Microstructures with compressive residual stress have also been preferential for forming dense oxide passive films and diminishing fatigue degradation generated from local corrosion occurrence [56]. Furthermore, cracking is more easily propagated under the presence of residual tensile stress than compressive ones [58].

The increment in residual stress in the deformed samples compared to the IC sample was congruent with the peak broadening from Fig. 6. The global residual stress horizontal tendency for the IC sample (Fig. 9) agreed with Fig. 4a due to the suggestion of a defects-free IC microstructure resulting from its thermo-mechanical process. Besides, the lower grain refinement in the R sample compared to that of the A sample (Fig. 3b,c) agreed with the highest ε and more compressive tendency in the A sample, as well as with the small alteration of crystalline domains on the R sample (Fig. 4b). Based on the above, the residual stress evaluation agreed with the previously explained findings. It is expected that these residual stresses vary with the depth. However, the surface residual stress will strongly influence the cracking initiation, which starts at the surface. These residual stress measurements are considered qualitative because they were done in the raw surface of the processed samples, being a convolution between the effect of the friction between the sample and the dies, and the effect of each deformation process. Considering the ε is accumulative, it is expected that the AR and RA samples will have an increment in residual stress. However, it could be affected due to the highly heterogeneous nature of the RCS process.

4. Conclusions

The application of four different deformation routes on the Al-7075 alloy, namely accumulative roll bonding, ARB (A),

repetitive corrugation and straightening, RCS (R), RCS + ARB (RA), and ARB + RCS (AR), produced different microstructures, texture, mechanical properties, and stress corrosion cracking (SCC) susceptibility. Compared to the initial condition (average grain size of 126 μm), the order from larger to lower grain refinement produced by the four routes was AR (1.2 μm) > A (3.2 μm) > RA (3.7 μm) > R (83.1 μm). All processed samples resulted in unimodal and widened grain size distributions of micro-, submicro- and nano-metric dimensions. The study of the crystallographic orientation showed that route R did not generate new orientation on the crystals, while a high density of preferred oriented crystals in different orientations were obtained for routes A, RA, and AR. The mechanical properties improvement agreed with the microstructural findings following the order: AR > RA > A > R. The SCC susceptibility also showed a slight enhancement with the four deformation routes. This fact might be related to the low chemical potential gradient produced by the grains of diverse size orders randomly distributed through the samples and the better continuity and adherence of the passive layer in fine-grained materials than coarse ones. Comparing the cracks per cm^2 obtained in the processed samples, the order of improvement of SCC susceptibility concerning the IC was R > A > AR > RA. Based on the above, the best combination of microstructural, mechanical, and SCC properties for just one deformation pass was obtained by applying the ARB process. All previous results demonstrated that the order of application of the ARB and RCS processes played an important role in the final properties of the AA7075.

Funding

This work was supported by Programa de Apoyo a Proyectos de Investigación e Innovación Tecnológica (PAPIIT)-UNAM under grant number IN102321.

Data availability

The data related to this manuscript would be made available on request.

Declaration of Competing Interest

The authors declare that they have no known competing financial interests or personal relationships that could have appeared to influence the work reported in this paper.

Acknowledgments

L. R–R. acknowledges CONACYT for the scholarship granted under the numbers 465504 and 308270. L. R–R. also acknowledges to the Universitat Politècnica de València (UPV) and Universitat Politècnica de Catalunya for the materials and equipment provided. G.G. acknowledges UNAM-DGAPA-PASPA program for funding the sabbatical year at the UPV. Valuable technical support by A. Tejeda-Cruz, O. Novelo-Peralta, E. Hernández-Mecinas, G. A. Lara-Rodríguez, J. Romero-Ibarra, R. Ibarra-Contreras, A. Bobadilla-Valencia, and C. Flores-Morales is also acknowledged.

REFERENCES

[1] Zhu Y, Chappuis LB, De Kleine R, Kim HC, Wallington TJ, Luckey G, et al. The coming wave of aluminum sheet scrap from vehicle recycling in the United States. Resour Conserv Recycl 2021;164:105208. https://doi.org/10.1016/j.resconrec.2020.105208.

[2] George E, Totten DSM. Handbook of aluminum; physical metallurgy and processes, vol. 1. New York: United States of America; 2003. https://doi.org/10.1111/j.1939-0025.1969.tb02453.x.

[3] Kunal Ahuja SB. Aluminum flat products market size. Glob Mark Insights Inc; 2020. p. 273. https://www.gminsights.com/industry-analysis/aluminum-flat-products-market.

[4] Dursun T, Soutis C. Recent developments in advanced aircraft aluminium alloys. Mater Des 2014;56:862–71. https://doi.org/10.1016/j.matdes.2013.12.002.

[5] Hatamleh O, Singh PM, Garmestani H. Stress corrosion cracking behavior of peened friction stir welded 2195 aluminum alloy joints. J Mater Eng Perform 2009;18:406–13. https://doi.org/10.1007/s11665-008-9303-8.

[6] Wang JT, Zhang YK, Chen JF, Zhou JY, Ge MZ, Lu YL, et al. Effects of laser shock peening on stress corrosion behavior of 7075 aluminum alloy laser welded joints. Mater Sci Eng, A 2015;647:7–14. https://doi.org/10.1016/j.msea.2015.08.084.

[7] Pandey V, Singh JK, Chattopadhyay K, Srinivas NCS, Singh V. Influence of ultrasonic shot peening on corrosion behavior of 7075 aluminum alloy. J Alloys Compd 2017;723:826–40. https://doi.org/10.1016/j.jallcom.2017.06.310.

[8] Al-Obaid YF. The effect of shot peening on stress corrosion cracking behaviour of 2205-duplex stainless steel. Eng Fract Mech 1995;51:19–25. https://doi.org/10.1016/0013-7944(94)00213-2.

[9] Dai K, Shaw L. Comparison between shot peening and surface nanocrystallization and hardening processes. Mater Sci Eng, A 2007;463:46–53. https://doi.org/10.1016/j.msea.2006.07.159.

[10] Thangapandian N, Balasivanandha Prabu S, Padmanabhan KA. Effect of temperature on grain size in AA6063 aluminum alloy subjected to repetitive corrugation and straightening. Acta Metall Sin (English Lett 2019;32:835–44. https://doi.org/10.1007/s40195-018-0866-6.

[11] Glaeser WA. A study of residual stress induced during rolling. J Tribol 1969;91:655–6. https://doi.org/10.1115/1.3555020.

[12] Alvand M, Naseri M, Borhani E, Abdollah-Pour H. Nano/ultrafine grained AA2024 alloy processed by accumulative roll bonding: a study of microstructure, deformation texture and mechanical properties. J Alloys Compd 2017;712:517–25. https://doi.org/10.1016/j.jallcom.2017.04.117.

[13] Roy S, Satyaveer Singh D, Suwas S, Kumar S, Chattopadhyay K. Microstructure and texture evolution during accumulative roll bonding of aluminium alloy AA5086. Mater Sci Eng, A 2011;528:8469–78. https://doi.org/10.1016/j.msea.2011.07.042.

[14] Hidalgo-Manrique P, Cepeda-Jiménez CM, Orozco-Caballero A, Ruano OA, Carreño F. Evolution of the microstructure, texture and creep properties of the 7075 aluminium alloy during hot accumulative roll bonding. Mater Sci Eng, A 2014;606:434–42. https://doi.org/10.1016/j.msea.2014.03.105.

[15] Guan RG, Tie D. A review on grain refinement of aluminum alloys: progresses, challenges and prospects. Acta Metall Sin (English Lett 2017;30:409–32. https://doi.org/10.1007/s40195-017-0565-8.
[16] Thangapandian N, Balasivanandha Prabu S, Padmanabhan KA. Effect of temperature and velocity of pressing on grain refinement in AA5083 aluminum alloy during repetitive corrugation and straightening process. Metall Mater Trans A Phys Metall Mater Sci 2016;47:6374–83. https://doi.org/10.1007/s11661-016-3811-1.
[17] Elizalde S, Ezequiel M, Figueroa IA, Cabrera JM, Braham C, Gonzalez G. Microstructural evolution and mechanical behavior of an Al-6061 alloy processed by repetitive corrugation and straightening. Metals 2020;10. https://doi.org/10.3390/met10040489.
[18] Romero-Resendiz L, Amigo-Borras V, Vicente-Escuder A, Elizalde S, Cabrera JM, Pineda-Ruiz D, et al. Effect of the microstructure generated by Repetitive Corrugation and Straightening (RCS) process on the mechanical properties and stress corrosion cracking of Al-7075 alloy. J Mater Res Technol 2021;15:4564–72. https://doi.org/10.1016/j.jmrt.2021.10.043.
[19] Su L, Lu C, Li H, Deng G, Tieu K. Investigation of ultrafine grained AA1050 fabricated by accumulative roll bonding. Mater Sci Eng, A 2014;614:148–55. https://doi.org/10.1016/j.msea.2014.07.032.
[20] Rezaee-Bazzaz A, Ahmadian S, Reihani H. Modeling of microstructure and mechanical behavior of ultra fine grained aluminum produced by accumulative roll-bonding. Mater Des 2011;32:4580–5. https://doi.org/10.1016/j.matdes.2011.04.011.
[21] Pandey SC, Joseph MA, Pradeep MS, Raghavendra K, Ranganath VR, Venkateswarlu K, et al. A theoretical and experimental evaluation of repetitive corrugation and straightening: application to Al-Cu and Al-Cu-Sc alloys. Mater Sci Eng, A 2012;534:282–7. https://doi.org/10.1016/j.msea.2011.11.070.
[22] Rajinikanth V, Arora G, Narasaiah N, Venkateswarlu K. Effect of repetitive corrugation and straightening on Al and Al-0.25Sc alloy. Mater Lett 2008;62:301–4. https://doi.org/10.1016/j.matlet.2007.05.014.
[23] Wei W, Wei KX, Du QB. Corrosion and tensile behaviors of ultra-fine grained Al-Mn alloy produced by accumulative roll bonding. Mater Sci Eng, A 2007;454–455:536–41. https://doi.org/10.1016/j.msea.2006.11.063.
[24] Gashti SO, Fattah-alhosseini A, Mazaheri Y, Keshavarz MK. Microstructure, mechanical properties and electrochemical behavior of AA1050 processed by accumulative roll bonding (ARB). J Alloys Compd 2016;688:44–55. https://doi.org/10.1016/j.jallcom.2016.07.177.
[25] Alvandi H, Farmanesh K. Microstructural and mechanical properties of nano/ultra-fine structured 7075 aluminum alloy by accumulative roll-bonding process. Procedia Mater Sci 2015;11:17–23. https://doi.org/10.1016/j.mspro.2015.11.020.
[26] Ezequiel M, Elizalde S, Cabrera JM, Picas J, Figueroa IA, Alfonso I, et al. Formability of the 5754-Aluminum alloy deformed by a modified repetitive corrugation and straightening process. Materials 2020;13:1–12. https://doi.org/10.3390/ma13030633.
[27] Edalati K, Horita Z. Significance of homologous temperature in softening behavior and grain size of pure metals processed by high-pressure torsion. Mater Sci Eng, A 2011;528:7514–23. https://doi.org/10.1016/j.msea.2011.06.080.
[28] Hidalgo-Manrique P, Cepeda-Jiménez CM, Ruano OA, Carreño F. Effect of warm accumulative roll bonding on the evolution of microstructure, texture and creep properties in the 7075 aluminium alloy. Mater Sci Eng, A 2012;556:287–94. https://doi.org/10.1016/j.msea.2012.06.089.
[29] Tsuji N, Saito Y, Lee SH, Minamino Y. ARB (accumulative roll-bonding) and other new techniques to produce bulk ultrafine grained materials. Adv Eng Mater 2003;5:338–44. https://doi.org/10.1002/adem.200310077.
[30] Bachmann F, Hielscher R, Schaeben H. Texture analysis with MTEX- Free and open source software toolbox. Solid State Phenom 2010;160:63–8. https://doi.org/10.4028/www.scientific.net/SSP.160.63.
[31] Dieter GE. Mechanical metallurgy. London: McGraw-Hill; 1988.
[32] International Standard ISO 9591. Corrosion of aluminium alloys — determination of resistance to stress corrosion cracking. 2004. 2004.
[33] Hutchinson B. The cube texture revisited. Mater Sci Forum 2012;702–703:3–10. https://doi.org/10.4028/www.scientific.net/MSF.702-703.3.
[34] Kallend JS, Davies GJ. A simulation of texture development in F.C.C. metals. Philos Mag 1972;25:471–90. https://doi.org/10.1080/14786437208226817.
[35] Faraji G, Kim HS, Kashi HT. Fundamentals of severe plastic deformation. Sev Plast Deform 2018;19–36. https://doi.org/10.1016/b978-0-12-813518-1.00001-1.
[36] Donadille C, Valle R, Dervin P, Penelle R. Development of texture and microstructure during cold-rolling and annealing of FCC alloys: example of an austenitic stainless steel. Acta Metall 1989;37:1547–71. https://doi.org/10.1016/0001-6160(89)90123-5.
[37] Shaeri MH, Shaeri M, Salehi MT, Seyyedein SH, Abutalebi MR. Effect of equal channel angular pressing on aging treatment of Al-7075 alloy. Prog Nat Sci Mater Int 2015;25:159–68. https://doi.org/10.1016/j.pnsc.2015.03.005.
[38] Vega MCV, Bolmaro RE, Ferrante M, Sordi VL, Kliauga AM. The influence of deformation path on strain characteristics of AA1050 aluminium processed by equal-channel angular pressing followed by rolling. Mater Sci Eng, A 2015;646:154–62. https://doi.org/10.1016/j.msea.2015.07.083.
[39] Zhao YH, Liao XZ, Jin Z, Valiev RZ, Zhu YT. Microstructures and mechanical properties of ultrafine grained 7075 Al alloy processed by ECAP and their evolutions during annealing. Acta Mater 2004;52:4589–99. https://doi.org/10.1016/j.actamat.2004.06.017.
[40] Muzyk M, Pakieła Z, Kurzydłowski KJ. Generalized stacking fault energies of aluminum alloys-density functional theory calculations. Metals 2018;8:12–4. https://doi.org/10.3390/met8100823.
[41] Zrnik J, Kovarik T, Novy Z, Cieslar M. Ultrafine-grained structure development and deformation behavior of aluminium processed by constrained groove pressing. Mater Sci Eng, A 2009;503:126–9. https://doi.org/10.1016/j.msea.2008.03.050.
[42] Valiev RZ. Structure and mechanical properties of ultrafine-grained metals. Mater Sci Eng, A 1997;234–236:59–66. https://doi.org/10.1016/s0921-5093(97)00183-4.
[43] Williamson GK, Hall WH. X-ray line broadening from filed aluminium and wolfram. Acta Metall 1953;1:22–31. https://doi.org/10.1016/0001-6160(53)90006-6.
[44] Kumar SSS, Raghu T. Strain path effects on microstructural evolution and mechanical behaviour of constrained groove pressed aluminium sheets. Mater Des 2015;88:799–809. https://doi.org/10.1016/j.matdes.2015.09.057.
[45] Paul H, Miszczyk MM. Deformation microstructure and texture transformations in FCC metals of medium-to-high stacking fault energy: critical role of micro- and macro-scale shear bands. Arch Metall Mater 2015;60:2235–46. https://doi.org/10.1515/amm-2015-0369.
[46] Chen P, Mao SC, Liu Y, Wang F, Zhang YF, Zhang Z, et al. In-situ EBSD study of the active slip systems and lattice rotation behavior of surface grains in aluminum alloy during tensile deformation. Mater Sci Eng, A 2013;580:114–24. https://doi.org/10.1016/j.msea.2013.05.046.

[47] Liu Q, Juul Jensen D, Hansen N. Effect of grain orientation on deformation structure in cold-rolled polycrystalline aluminium. Acta Mater 1998;46:5819–38. https://doi.org/10.1016/S1359-6454(98)00229-8.
[48] Tang J, Zhang Y, Ye L, Qu M, Wu J, Zhang Z, et al. Effect of grain boundary and crystallographic orientation on the stress corrosion behavior of an Al-Zn-Mg alloy. J Mater Eng Perform 2019;28:2954–66. https://doi.org/10.1007/s11665-019-04050-x.
[49] Zhao YH, Liao XZ, Cheng S, Ma E, Zhu YT. Simultaneously increasing the ductility and strength of nanostructured alloys. Adv Mater 2006;18:2280–3. https://doi.org/10.1002/adma.200600310.
[50] Zhao Y, Liu J, Topping TD, Lavernia EJ. Precipitation and aging phenomena in an ultrafine grained Al-Zn alloy by severe plastic deformation. J Alloys Compd 2021;851:156931. https://doi.org/10.1016/j.jallcom.2020.156931.
[51] Zhao YH, Liao XZ, Zhu YT, Valiev RZ. Enhanced mechanical properties in ultrafine grained 7075 Al alloy. J Mater Res 2005;20:288–91. https://doi.org/10.1557/JMR.2005.0057.
[52] Alvarado EE, Figueroa IA, Gonzalez G. Microstructural and mechanical analysis of an 1100 aluminum alloy processed by repetitive corrugation and straightening. Phys Met Metallogr 2020;121:1319–25. https://doi.org/10.1134/S0031918X20130025.
[53] Gollapudi S. Grain size distribution effects on the corrosion behaviour of materials. Corrosion Sci 2012;62:90–4. https://doi.org/10.1016/j.corsci.2012.04.040.
[54] Wang L, Lin Y, Zeng Z, Liu W, Xue Q, Hu L, et al. Electrochemical corrosion behavior of nanocrystalline Co coatings explained by higher grain boundary density. Electrochim Acta 2007;52:4342–50. https://doi.org/10.1016/j.electacta.2006.12.009.
[55] Ralston KD, Birbilis N. Effect of grain size on corrosion: a review. Corrosion 2010;66:750051–7500513. https://doi.org/10.5006/1.3462912.
[56] Abdulstaar M, Mhaede M, Wagner L, Wollmann M. Corrosion behaviour of Al 1050 severely deformed by rotary swaging. Mater Des 2014;57:325–9. https://doi.org/10.1016/j.matdes.2014.01.005.
[57] Zhang W, Frankel GS. Anisotropy of localized corrosion in AA2024-T3. Electrochem Solid State Lett 2000;3:268–70. https://doi.org/10.1149/1.1391121.
[58] Li J, Li F, Li J, Liang S. Crack-induced intergranular corrosion behavior of aerial aluminum alloy subjected to severe plastic deformation. Mater Corros 2019;70:234–45. https://doi.org/10.1002/maco.201810150.
[59] Orłowska M, Ura-Bińczyk E, Olejnik L, Lewandowska M. The effect of grain size and grain boundary misorientation on the corrosion resistance of commercially pure aluminium. Corrosion Sci 2019;148:57–70. https://doi.org/10.1016/j.corsci.2018.11.035.
[60] Prevéy PS, Research L. Current applications of X-ray diffraction residual stress measurement. Dev Mater Charact Technol 1996;103–10.